

NeuralRoom: Geometry-Constrained Neural Implicit Surfaces for Indoor Scene Reconstruction

YUSEN WANG, School of Computer Science, Wuhan University, China
 ZONGCHENG LI, School of Computer Science, Wuhan University, China
 YU JIANG, School of Computer Science, Wuhan University, China
 KAIXUAN ZHOU, Riemann Lab, Huawei, China
 TUO CAO, School of Computer Science, Wuhan University, China
 YANPING FU, School of Computer Science and Technology, Anhui University, China
 CHUNXIA XIAO*, School of Computer Science, Wuhan University, China

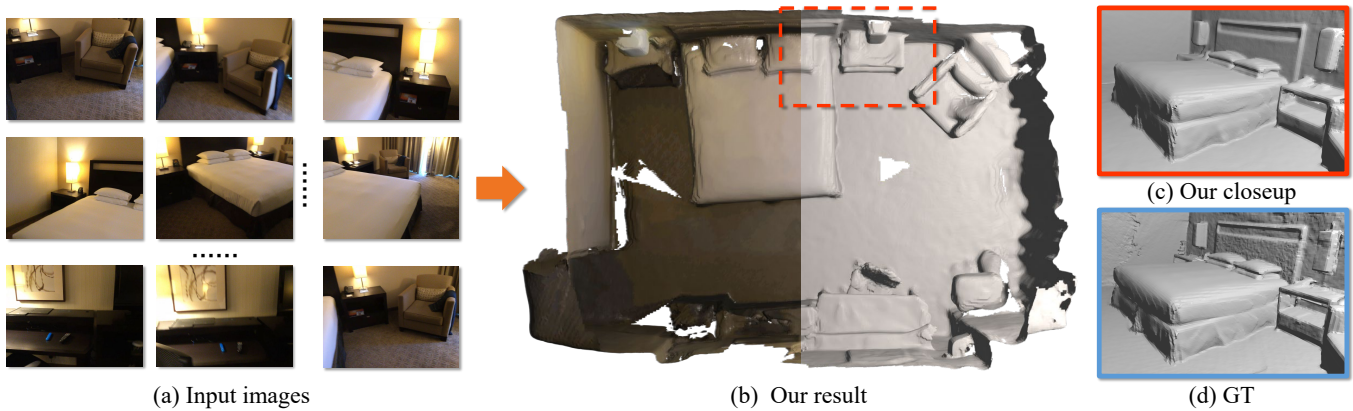


Fig. 1. We present a system called NeuralRoom for reconstructing a room-sized indoor scene from 2D images. There are many texture-less regions in indoor scenes, making conventional multiview stereo methods fail in reconstruction. The implicit neural representation method has recently become a promising reconstruction method due to its simplicity and high reconstruction quality. However, shape-radiance ambiguity makes it unable to reconstruct indoor scenes well. NeuralRoom effectively integrates normal and depth information to overcome ambiguity, which guarantees reconstruction details and completeness.

We present a novel neural surface reconstruction method called NeuralRoom for reconstructing room-sized indoor scenes directly from a set of 2D images. Recently, implicit neural representations have become a promising way to reconstruct surfaces from multiview images due to their high-quality results and simplicity. However, implicit neural representations usually cannot reconstruct indoor scenes well because they suffer severe shape-radiance ambiguity. We assume that the indoor scene consists of texture-rich and flat texture-less regions. In texture-rich regions, the multiview stereo can obtain accurate results. In the flat area, normal estimation networks usually obtain a good normal estimation. Based on the above observations, we reduce the possible spatial variation range of implicit neural surfaces by reliable geometric priors to alleviate shape-radiance ambiguity. Specifically, we use multiview stereo results to limit the NeuralRoom optimization space and then use reliable geometric priors to guide NeuralRoom training. Then the NeuralRoom would produce a neural scene representation that can render an image consistent with the input training images. In addition, we propose a smoothing method called perturbation-residual restrictions to improve

*Corresponding author

Authors' addresses: Yusen Wang, School of Computer Science, Wuhan University, Wuhan, China, wangyusen@whu.edu.cn; Zongcheng Li, School of Computer Science, Wuhan University, Wuhan, China; Yu Jiang, School of Computer Science, Wuhan University, Wuhan, China; Kaixuan Zhou, Riemann Lab, Huawei, Wuhan, China; Tuo Cao, School of Computer Science, Wuhan University, Wuhan, China; Yanping Fu, School of Computer Science and Technology, Anhui University, Hefei, China; Chunxia Xiao, School of Computer Science, Wuhan University, Wuhan, China.

the accuracy and completeness of the flat region, which assumes that the sampling points in a local surface should have the same normal and similar distance to the observation center. Experiments on the ScanNet dataset show that our method can reconstruct the texture-less area of indoor scenes while maintaining the accuracy of detail. We also apply NeuralRoom to more advanced multiview reconstruction algorithms and significantly improve their reconstruction quality.

CCS Concepts: • **Computing methodologies** → **Reconstruction**.

Additional Key Words and Phrases: Neural Implicit Representation, Indoor Scene Reconstruction, Multiview Reconstruction

1 INTRODUCTION

Reconstructing 3D geometries from multiview images is a fundamental topic in computer vision and graphics. The reconstructed model can be applied to VR/AR, video games, 3D printing and CAD manufacturing. Reconstruction of outdoor scenes and single objects with rich textures has been widely studied. However, few studies on indoor multiview reconstruction are directly based on color images. Objects in indoor scenes are usually of a single color, such as walls, furniture, and floors, which cannot be well restricted by photometric consistency.

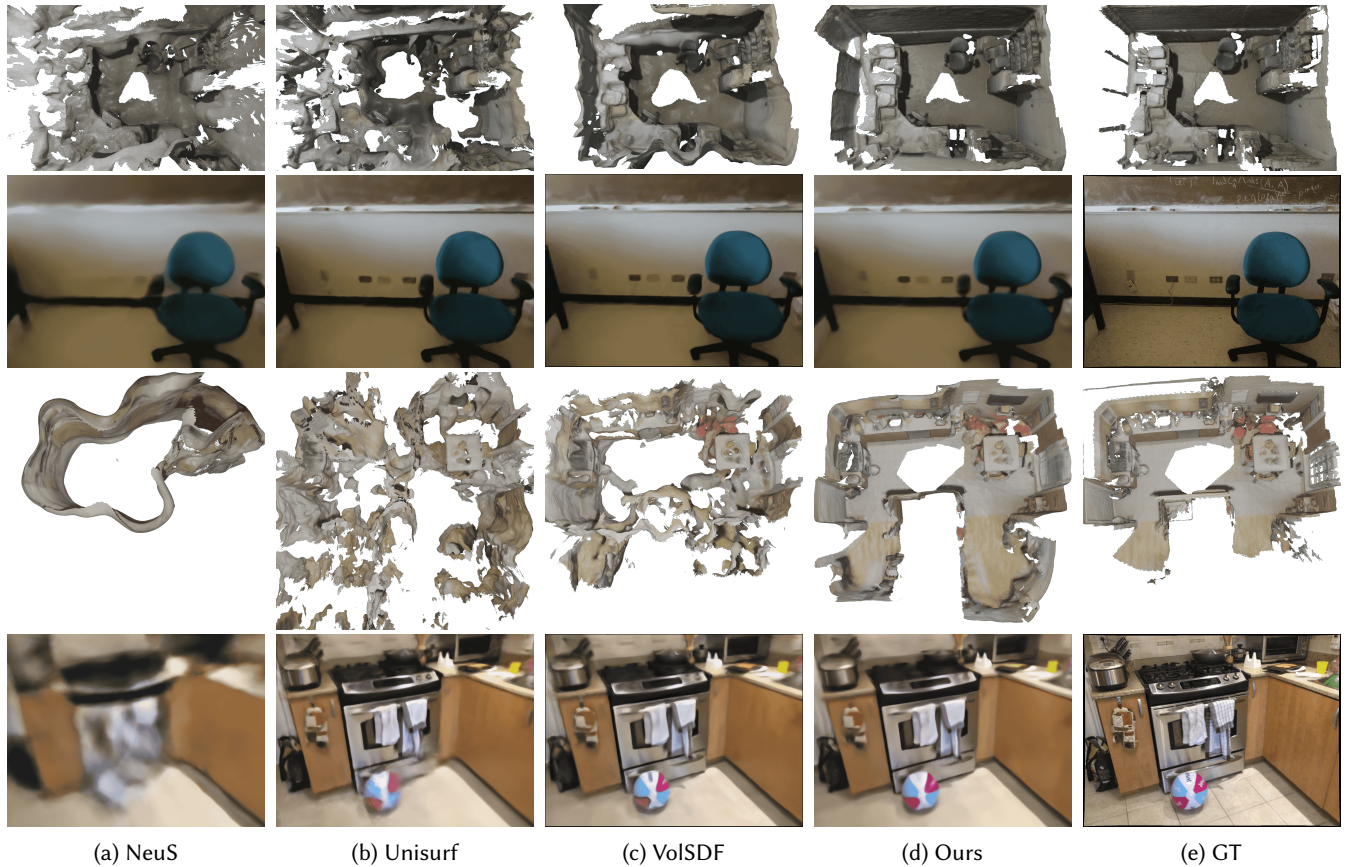


Fig. 2. Inherent shape-radiance ambiguity. For each set of results, the first row shows the reconstruction results. The second row shows rendering results from the implicit neural representation. State-of-the-art methods [Oechsle et al. 2021; Wang et al. 2021b; Yariv et al. 2021] can yield impressive high-quality reconstruction of a single object, while they often yield unsatisfactory reconstruction and rendering results for indoor scenes. Optimization of implicit neural representations easily falls into a local optimum, which will result in an incorrect reconstruction or even fail in reconstruction.

MVS reconstruction algorithms have difficulty performing feature matching on texture-less areas, which leads to incompleteness and a large number of outliers.

Learning-based per-view depth estimation methods can obtain a good depth estimation for a single image. However, although it has good performance in quantitative evaluation, the fused 3D model is usually inaccurate due to the lack of consistency constraints between views. In addition, the areas with sudden depth changes are usually oversmoothed.

Another kind of learning-based reconstruction method directly extracts a 3D mesh from a volumetric representation. [Murez et al. 2020; Sun et al. 2021a] obtained effective reconstruction of indoor scenes. The reconstruction results of these methods generally have better completeness, but the scene details need to be further improved.

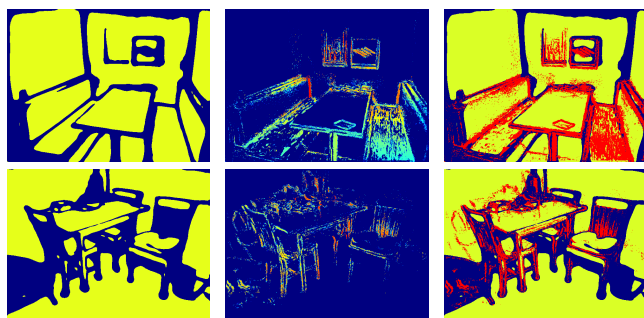
Recently, neural surface reconstruction methods have significantly promoted the development of 3D reconstruction, which achieves better reconstruction quality than conventional reconstruction approaches. In addition, these methods have the potential

to reconstruct objects with non-Lambertian, less observed regions and complex geometry.

NeRF-based methods [Mildenhall et al. 2020] learn a function that maps 3D coordinates and 2D viewing directions to opacity and color values. However, since additional viewing directions need to be an additional input, the solution is not unique to explaining the input training images when lacking explicit or implicit regularization. Such a situation is called shape-radiance ambiguity [Buehler et al. 2001; Chai et al. 2000; Debevec et al. 1996; Zhang et al. 2020a], which means incorrect geometry can render an image consistent with the input training image. Shape-radiance ambiguity becomes the bottleneck in the reconstruction of indoor scenes for rendering-based surface reconstruction methods (Figure 2), although these methods [Oechsle et al. 2021; Wang et al. 2021b; Yariv et al. 2021] yield impressive reconstruction results on a single object.

In this work, we propose a novel neural surface reconstruction method called NeuralRoom to assign appropriate global and local constraints between sampling rays to overcome shape-radiance ambiguity. We assume that the indoor scene is composed of two

parts. The first part contains rich textured areas and edges such as object edges and various color decorations. The other part contains texture-less regions, such as walls and ground. We found that MVS can obtain high-precision estimates in textured areas but obtain relatively inaccurate results in texture-less areas. In contrast, neural network-based normal estimation methods [Bae et al. 2021; Do et al. 2020; Huang et al. 2019; Wang et al. 2020] always obtain a good estimation on flat areas but obtain inaccurate results on edges and rich textured areas (Figure 3). In our method, we combine their advances and propose a new smoothing term to alleviate shape-radiance ambiguity.



(a) Normal prior area (b) Distance prior area (c) Priors overlap

Fig. 3. Different areas in which priors take effect on. (a) shows the flat regions constrained by a reliable normal prior filtered by uncertainty, which is provided by [Bae et al. 2021]. (b) shows the rich texture and edge regions constrained by the distance prior provided by COLMAP [Schonberger and Frahm 2016]. (c) shows the overlapping area of (a) and (b). The rich texture regions and edges can have a good depth estimation. The texture-less regions can have an accurate normal estimation. The reliable depth and normal information are used to guide the optimization of neural implicit representation.

Specifically, our system consists of two main stages. The first stage is geometry prior acquisition (Figure 5). We use multiview stereo to calculate the depth map and bounding box based on the depth fusion result. Then, we generate the distance prior from the depth map of each view. In addition, we use a learning-based normal estimation network to predict the normal map and filter it with uncertainty. The distance prior and normal prior are used to guide the next stage NeuralRoom differentiable renderer.

The NeuralRoom renderer takes the above priors to optimize the implicit neural surface. The distance prior ensures the accuracy of reconstructed details and the normal prior limits the geometry feature of the texture-less region. To further improve the reconstruction quality of the flat regions, we conduct a smoothing method called perturbation-residual restriction for our NeuralRoom renderer. We assume that the sampling points on the local surface should be close to each other. If the local area is flat, the normal of sampling points should be the same.

Our main contributions are the following:

- Propose NeuralRoom, a novel neural surface reconstruction pipeline, for reconstructing indoor scenes. Researchers can

use their own more advanced estimation methods which can yield more accurate priors and differentiable renderers to achieve better reconstruction results.

- Introduce several efficient geometric priors for overcoming shape-radiance ambiguity. The distance prior acquired by MVS helps improve the detail accuracy. The normal prior helps enhance the completeness and accuracy of the texture-less region.
- Develop perturbation-residual restrictions working as smoothing terms to improve the accuracy and completeness of the flat and texture-less regions. There are some noise data in the priors, so this smoothing term can further enhance the reconstruction quality.

Experimental results on the ScanNet dataset show that we have successfully applied multiview neural surface reconstruction for indoor scene reconstruction. Our complete framework has significantly improved state-of-the-art multiview reconstruction results on the tested indoor scenes. In addition, we use mobile phones to take photos of real-world scenes and successfully use our proposed system for reconstruction.

2 RELATED WORK

2.1 Multiview Reconstruction

Multiview reconstruction aims to reconstruct the three-dimensional geometric model of the scene from a set of images with or without calibrated camera poses. The key point of the image-based approach is photometric consistency assumptions. Among all kinds of methods, depth-map merging-based methods are the most widely used.

Multiview stereo has been widely studied [Seitz et al. 2006]. Traditional MVS methods [Galliani et al. 2015; Schonberger and Frahm 2016; Xu and Tao 2019] estimate the corresponding depth map for each input high-resolution image offline and then fuse it into the final three-dimensional model [Bernardini et al. 1999; Kazhdan et al. 2006; Merrell et al. 2007]. These MVS methods often use the idea of sampling and propagation in PatchMatch to make depth estimation more effective. The learning based MVS approaches [Chen et al. 2019; Cheng et al. 2020; Ding et al. 2021; Gu et al. 2020; Kuhn et al. 2020; Wang et al. 2021a; Wei et al. 2021b; Xu et al. 2021; Yan et al. 2020; Yang et al. 2020; Yao et al. 2018, 2019; Zhang et al. 2020b] have become popular in recent years and have shown some advantages in terms of accuracy and completeness in specific datasets. Most of the deep learning methods take MVSNet [Yao et al. 2018] as their skeleton and are based on plane-sweep stereo [Collins 1996]. They use a convolutional neural network to extract higher dimensional 2D features in the image, usually following a 3D convolution to regress the depth for per pixel. The 3D CNN is time- and memory-consuming due to the large number of parameters. The following works adopt a pyramid structure [Cheng et al. 2020; Gu et al. 2020; Liao et al. 2021; Yang et al. 2020] or recurrent network [Wei et al. 2021b; Yan et al. 2020; Yao et al. 2019] to reduce the memory consumption. Some other work integrates PatchMatch [Wang et al. 2021a], uncertainty [Zhang et al. 2020b], attention mechanism [Ding et al. 2021], semantic segmentation [Xu et al. 2021] and other mechanisms [Chen et al. 2019; Kuhn et al. 2020] into MVS approaches.

For indoor scenes, because there are a large number of weak texture areas in the scene, such as walls, floors and solid color furniture, the correspondence matching quality of MVS is usually poor, which leads to missing parts and outliers in the reconstruction. Previous works have attempted to reconstruct texture-less regions with different methods, such as multiresolution [Xu and Tao 2019], planar priors [Sun et al. 2021b; Xu and Tao 2020a], and depth map completion [Kuhn et al. 2020; Liu et al. 2020b]. These methods can improve the reconstruction results of the texture-less region to a certain extent and are better than the conventional methods in quantitative evaluation. However, they still cannot obtain a satisfactory result in the indoor scene.

Some learning-based multiview depth estimation and SLAM methods [Hou et al. 2019; Jiang et al. 2021; Long et al. 2021a,b; Rich et al. 2021; Teed and Deng 2018; Wang and Shen 2018] use data-driven methods to reduce the over-reliance on the photometric consistency assumption. They can quickly produce a low-resolution dense depth map. These methods can assign depth values to texture-less areas, but the areas with sudden depth changes are often oversmoothed. The 3D model acquired by TSDF fusion can show the general appearance of the scene, while the accuracy is poor. In addition, after obtaining the raw reconstruction through MVS, object or scene completion algorithms [Bokhovkin and Dai 2022; Dai et al. 2020, 2021; Zhang et al. 2022] can be used to complete and optimize the scene.

2.2 Implicit Neural Representation

Implicit neural representations represent scenes as a continuous implicit function, which can represent high-resolution geometries in finite memory. This implicit representation has been successfully used in novel view synthesis [Barron et al. 2021; Liu et al. 2020a; Mildenhall et al. 2020; Müller et al. 2022; Niemeyer et al. 2021; Roessle et al. 2021; Tancik et al. 2022; Xiangli et al. 2021; Xu et al. 2022a; Yu et al. 2021], shape representation [Atzmon et al. 2019; Atzmon and Lipman 2020; Genova et al. 2019; Mescheder et al. 2019; Michalkiewicz et al. 2019; Müller et al. 2022; Park et al. 2019; Peng et al. 2020], human reconstruction [Saito et al. 2019, 2020], relighting [Philip et al. 2021], and multiview 3D reconstruction [Niemeyer et al. 2020; Oechsle et al. 2021; Wang et al. 2021b; Xu et al. 2022b; Yariv et al. 2020].

[Choy et al. 2016; Ji et al. 2017, 2020; Kar et al. 2017; Murez et al. 2020; Sun et al. 2021a] presented end-to-end 3D reconstruction methods that use a global volumetric representation to assemble features from all views and then predict the 3D model directly from the feature volume. [Liu et al. 2020a; Murez et al. 2020] presented learning-based dense reconstruction methods for indoor scenes that can obtain better reconstruction than the previous methods in terms of quality and quantitative comparison. However, the details of the reconstruction results need to be improved.

Recently, differentiable rendering multiview 3D reconstruction methods have significantly advanced the development of 3D reconstruction and achieve better reconstruction quality than other conventional reconstruction methods on a single object. There are two types of rendering methods: surface rendering methods [Kellnhofer

et al. 2021; Niemeyer et al. 2020; Yariv et al. 2020] and volume rendering methods [Mildenhall et al. 2020; Müller et al. 2022; Oechsle et al. 2021; Wang et al. 2021b; Yu et al. 2021]. Surface rendering-based methods assume that the radiance of a ray required for rendering is only related to the intersection of the ray and the geometric surface. This makes the gradient only backpropagated to the local area at the intersection. These methods usually cannot deal with complex geometries well and rely heavily on the object’s mask. When the mask is missing, reconstruction usually fails. Volume rendering-based methods assume that the rendering color is related to the radiance and the corresponding alpha weight at all spatial locations through which the ray passes. Therefore, the gradient can be backpropagated to all sites involved in rendering. These methods can reconstruct complex scenes without a mask and deal with some scenes with sudden depth changes. However, it is usually unable to obtain high-precision geometric surfaces, especially for the texture-less region, due to the lack of geometric surface constraints. In addition, the reconstruction may contain conspicuous noises.

The rendering-based implicit neural representation shows the potential to replace traditional MVS reconstruction. However, its performance is not as good as that of traditional reconstruction methods in indoor scenes. NeRF-based methods [Mildenhall et al. 2020] map a 5D input (3D coordinates plus the 2D viewing direction) to opacity and color values, which easily suffers from inherent shape-radiance ambiguity due to the additional input dimensions and the lack of implicit or explicit regularization in the implicit representation.

Many works use the depth value as a constraint to alleviate this ambiguity [Chen et al. 2021; Roessle et al. 2021; Wei et al. 2021a; Xu et al. 2022a] in their respective fields. [Roessle et al. 2021; Wei et al. 2021a] used the monocular depth estimation network optimized by MVS results to provide a distance prior for each pixel to reduce shape-radiance ambiguity and improve the effect of indoor depth estimation and novel view synthesis. However, the consistency between views of depth estimation is far from sufficient to obtain a satisfactory 3D model.

The concurrent works [Guo et al. 2022; Wang et al. 2022; Yu et al. 2022] have ideas similar to those of our work. These methods use depth estimation to provide depth cues and use normal information as additional constraints to reconstruct indoor scenes.

3 OVERVIEW

Shape-radiance ambiguity [Buehler et al. 2001; Chai et al. 2000; Debevec et al. 1996; Zhang et al. 2020a] often exists in the Nerf-based rendering method [Mildenhall et al. 2020]. A well-trained implicit neural representation can achieve suitable outgoing 2D radiance at each wrong geometry surface point to perfectly fit a set of training images, as shown in Figure 2. However, for the indoor scene, rectifying this ambiguity faces several challenges:

- Inaccurate camera pose.
- Unstable light condition and photo imaging quality.
- Many texture-less areas.
- Inside-out shooting which makes some areas only visible from almost the same direction.
- Large optimization space.

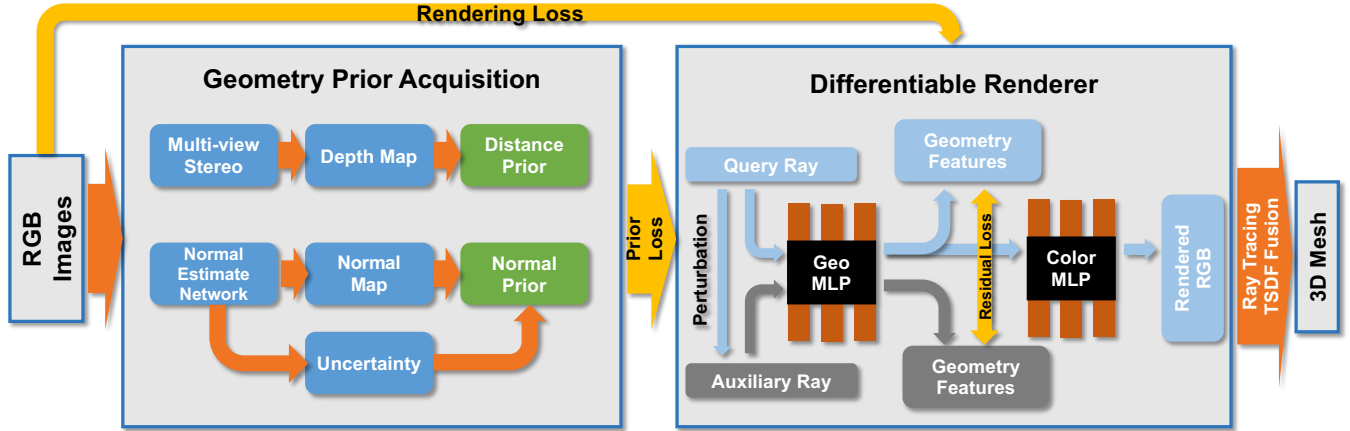


Fig. 4. Method overview. The goal of our system is to reconstruct indoor scenes directly from RGB images with known camera parameters. The system consists of two parts. First, we use the multiview stereo method [Schonberger and Frahm 2016] and the normal estimate network [Bae et al. 2021] to acquire the geometry prior. The distance prior acquired from MVS ensures the accuracy of texture-rich and edge areas, while the normal prior ensures the completeness of the texture-less region. Then, we use these geometry prior and RGB images to guide the optimization of the NeuralRoom module, which is a volume rendering-based neural surface reconstruction method. In addition, in the NeuralRoom module, we propose perturbation-residual restriction to constrain the implicit surface. Finally, we use ray tracing on the reconstructed scene and perform TSDF fusion to obtain the final 3D mesh model.

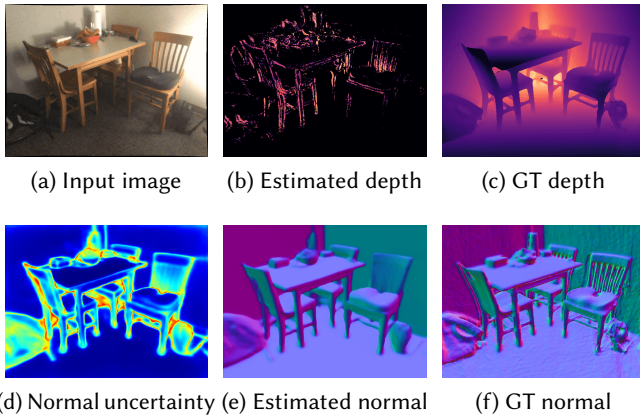


Fig. 5. Distance and normal priors. (a) Input RGB image. (b) Depth map estimated by COLMAP [Schonberger and Frahm 2016]. (c) Ground truth depth map in the ScanNet [Dai et al. 2017] dataset. (d) Uncertainty acquired by [Bae et al. 2021] indicating the corresponding normal estimation quality. The normal estimation result in the bright colored areas is inaccurate. (e) Normal map estimated by [Do et al. 2020]. (f) Ground truth normal map acquired by performing ray tracing on the ground truth mesh model.

We introduce a novel multiview neural surface reconstruction method called NeuralRoom, which aims to handle the shape-radiance ambiguity in indoor scenes. Given a relatively accurate camera pose and varied observation directions, we use appropriate geometry cues to guide the optimization of neural representations and avoid falling into a local optimum. Specifically, we divide the scene into the textured and texture-less regions according to geometric features. For the textured and edge areas, we use the distance prior acquired

by COLMAP [Schonberger and Frahm 2016], which is usually accurate. We give a high weight to make the implicit surface consistent with the distance prior. For flat and texture-less regions, we use the normal prior acquired by [Bae et al. 2021] to limit the local surface geometry. In addition, we propose smoothing terms called perturbation-residual restrictions to further improve the accuracy and completeness.

The method proceeds in three parts:

- Geometry prior acquisition. Section 4.1 introduces data preparation and how to acquire the distance and normal prior.
- NeuralRoom renderer. Section 4.2 and Section 4.3 introduce the NeuralRoom renderer and the perturbation-residual restrictions.
- Mesh extraction. Section 4.4 introduces our mesh extraction method.

4 METHOD

4.1 Preprocessing

Image Processing. First, we extract the images from the indoor video sequence. Usually, we would obtain thousands of photos. Because imaging quality will affect the accuracy of MVS, normal estimation, and rendering-based reconstruction, we use a Laplacian filter for blurring detection to determine which images should be used in the experiment. Given a set of images, we divided every ten images into a subgroup. Then we calculate the Laplacian of the source image as a blurring degree. Each subset leaves only one optimal image with the largest Laplacian in the subgroup. All optimal images generate the image set I we used in the experiment.

Distance Prior. In the textured areas and edges, MVS can obtain high accuracy results. We hope to ensure the accuracy of these areas in NeuralRoom. We run COLMAP [Schonberger and Frahm 2016],

a traditional multiview stereo method, on each selected image I_i with fixed camera intrinsic parameters K_i and extrinsic parameters $T_i = [R_i|t_i]$ to acquire a per-view depth map D_i^{MVS} . The depth map D_i^{MVS} has been filtered by geometric consistency and eroded by 3 pixels. We set the values to zero for pixels where the depth is not defined. Therefore, the acquired depth map D_i^{MVS} is sparser but more accurate.

We convert the depth to the distance between the camera center and the corresponding point for more convenient use in the optimization. We reproject the 2D coordinate to a 3D point in the world coordinate using D_i^{MVS} and corresponding parameters K_i and T_i :

$$X_i(p) = T_i^{-1}K_i^{-1}D_i^{MVS}(p)\tilde{p}, \text{ where } D_i^{MVS}(p) \neq 0, \quad (1)$$

where p is the 2D pixel coordinate in I_i , \tilde{p} is the homogeneous augmentation of p , X_i is corresponding 3D point.

Each scene has a different size and location in world coordinates. Therefore, we normalize the scene into a cube with the center at the origin and a side length of 2. First, we fuse all depth maps into a point cloud and compute an axis-aligned bounding box. Then, we obtain the minimum bounding point X_{min}^{BBox} and the maximum bounding point X_{max}^{BBox} . With X_{min}^{BBox} and X_{max}^{BBox} , we can define the center of the scene in the real world as the translation t_{opt} to the optimization coordinate. We then further define the scale s which compresses the longest side length of the bounding box by s times, so we ensure that the reconstructed scene falls into the NeuralRoom optimization space. Finally, we define the distance prior D_i as

$$D_i(p) = \|K_i^{-1}D_i^{MVS}(p)\tilde{p}\|/s, \text{ where } D_i^{MVS}(p) \neq 0. \quad (2)$$

Normal Prior and Uncertainty Acquisition. Texture-less regions cannot be effectively constrained by photometric consistency loss, which always suffers from shape-radiance ambiguity. Therefore, we use the surface normal acquired from the neural network to guide the optimization of NeuralRoom. We take UncertSurfaceNormal [Bae et al. 2021] as our normal estimation module. [Bae et al. 2021] is a learning-based normal estimation method. It takes a single image as input, and the output contains an estimated normal map and corresponding uncertainty map. We assume that the position with large uncertainty is where the surface geometry changes sharply. The area with a smooth surface generally has less uncertainty.

The learning-based approaches always take a normal map calculated by a depth map as ground truth which is captured by a depth sensor. However, there is usually noise in the depth map obtained by the depth sensor. The depth varies greatly on edges, and the depth of special material surfaces is typically unable to be collected. In addition, the depth map acquired by the depth sensor needs to be converted to the image sensor coordinate system through extrinsic parameters. This transform also causes the depth value to be missing at the boundary. Therefore, the estimation of edges is usually inaccurate. We need an indication to determine which parts of the normal estimation results are reliable. Edge detection may also be an effective indication. In our approach, we take the uncertainty map given by [Bae et al. 2021].

We feed the image I_i into [Bae et al. 2021] and obtain the normal estimation N_i^{raw} and corresponding uncertainty U_i . Then, we use uncertainty as an indication to filter N_i^{raw} to obtain a reliable

estimation result N_i :

$$N_i = N_i^{raw} \cdot Bool(U_i \leq mean(U_i)). \quad (3)$$

We take the mean value of U_i as the threshold to filter N_i^{raw} and obtain a reliable estimation result N_i . We also set a zero value for pixels where the normal is filtered. We use N_i as a normal prior to guide the optimization of NeuralRoom. In addition, the normal prior is also used in the perturbation-residual training method.

4.2 NeuralRoom Module

NeuralRoom Rendering Method. Our NeuralRoom renderer follows the basic volume rendering model NeuS [Wang et al. 2021b] while integrating additional prior information and the perturbation-residual restriction.

NeuralRoom uses two multilayer perceptrons (MLPs) to represent geometry f and color functions c . The geometry function $f: \mathbb{R}^3 \rightarrow \mathbb{R}$ maps point $x \in \mathbb{R}^3$ to the signed distance to the object. The color function $c: \mathbb{R}^3 \times \mathbb{S}^2 \rightarrow \mathbb{R}^3$ maps a point position $x \in \mathbb{R}^3$ and a viewing direction $v \in \mathbb{S}^2$ to the RGB color space. The surface \mathcal{S} of the object is represented by the zero set of its signed distance function (SDF):

$$\mathcal{S} = \{x \in \mathbb{R}^3 | f(x) = 0\}. \quad (4)$$

As a volume rendering method, the NeuralRoom renderer represents scenes as a colorized volume with weights and integrates radiance along with rays via alpha blending. Each pixel determines a ray. This scheme samples n points along the ray $r: \{x_i = o + t_i v | i = 1, 2, \dots, n, t_i < t_{i+1}\}$. o is the position from which the ray is emitted, which is usually the center of the camera. v is the direction of the ray. t is the length of the ray that has been emitted.

Substituting a query spatial position x_i into the geometry function f , an SDF estimation should be $f(x_i)$. Then, a unimodal density distribution function $\phi_s(f(x_i))$ is introduced. $\phi_s(x_i) = se^{-sx_i}/(1 + e^{-sx_i})^2$ which is the derivative of the sigmoid function $\Phi_s(x_i) = (1 + e^{-sx_i})^{-1}$, s is a learnable parameter. The discrete opacity values α are shown to be:

$$\alpha_i = \max\left(\frac{\Phi_s(f(x_i)) - \Phi_s(f(x_{i+1}))}{\Phi_s(f(x_i))}, 0\right). \quad (5)$$

The scheme approximates the color, normal, and length of this ray by calculating:

$$\hat{C}(r) = \sum_{i=1}^n M_i \alpha_i c(x_i, v), \quad (6)$$

$$\hat{D}(r) = \sum_{i=1}^n M_i \alpha_i t_i, \quad (7)$$

$$\hat{N}(r) = \sum_{i=1}^n M_i \alpha_i \text{gradient}(x_i), \quad (8)$$

where $M_i = \prod_{j=1}^{i-1} (1 - \alpha_j)$ indicates the accumulated transmittance, α_i is the per voxel opacity value acquired from implicit geometry function f , and $\hat{C}, \hat{D}, \hat{N}$ represent rendering color, rendering depth and rendering normal respectively. The derivative of implicit geometric function f with respect to the three coordinate directions at point p : $(\frac{\partial f}{\partial x}, \frac{\partial f}{\partial y}, \frac{\partial f}{\partial z})$ is the gradient at that position. The derivation process is completed by PyTorch's automatic derivation [Paszke et al. 2019].

Guided Optimization. Let p be the 2D pixel coordinate in I_i . To optimize NeuralRoom, we first sample some pixels from a specific image I_i and generate their corresponding rays in world space $P = \{C_i(p), D_i(p), N_i(p), o_i, v_i(p)\}$, where C_i is the color of the pixel acquired from I_i , D_i is the corresponding distance prior, which is the length between the camera center and the intersection of the surface, N_i is the corresponding normal prior in world coordinates, o_i is the camera center in world coordinates, and v_i is the ray direction. o_i and v_i are calculated from K_i and T_i^{opt} . We assume that the batch size of sampling rays is k , and we sample n points along each ray.

As a rendering-based neural surface reconstruction method, its most important loss function is to minimize the difference between the rendered pixel colors and the ground truth input corresponding pixel colors:

$$\mathcal{L}_{color} = \frac{1}{k} \sum_k |\hat{C}_k - C_k|, \quad (9)$$

where C_k is the corresponding pixel color, \hat{C}_k is the corresponding rendering color.

Prior Loss. The prior loss \mathcal{L}_{prior} consists of two parts, the distance prior loss \mathcal{L}_{prior_D} and the normal prior loss \mathcal{L}_{prior_N} :

$$\mathcal{L}_{prior} = \mathcal{L}_{prior_D} + \gamma \mathcal{L}_{prior_N}. \quad (10)$$

We force the distance \hat{D}_k between the camera center and the intersection of the ray and implicit surface to consist of the distance prior D_k . If a sampled ray has a corresponding distance prior, we perform the distance prior loss to constrain the intersection to a specific position:

$$\mathcal{L}_{prior_D} = \frac{1}{n} \sum_{j=1}^n \text{SmoothL1}(\hat{D}_k^j, D_k^j), \quad (11)$$

$$\text{SmoothL1}(A, B) = \begin{cases} 0.5 * \|A - B\|^2 / \text{beta}, & \|A - B\| \leq \text{beta}, \\ \|A - B\| - 0.5 * \text{beta} & \|A - B\| > \text{beta}, \end{cases} \quad (12)$$

where \hat{D}_k^j is the rendered depth if the pixel has a distance prior, A and B are two vectors of the same dimension used to illustrate SmoothL1 , SmoothL1 is the smooth L1 loss ($\text{beta} = 0.1$), D_k is the corresponding distance prior, and n is the number of rays that have a distance prior. Therefore, the intersection positions between these rays and the implicit surface are consistent with the distance prior. The distance prior makes the reconstruction results consistent with the MVS results in texture-rich areas and where the surface geometry changes sharply. In addition, since the rendering loss is dominant in the optimization process, this will reduce the impact of outliers in MVS results on reconstruction.

Next, we need to solve the most important problem of indoor reconstruction: shape-radiance ambiguity in the texture-less region. The normal prior loss is:

$$\mathcal{L}_{prior_N} = \frac{1}{n} \sum_{j=1}^n \text{SmoothL1}(\hat{N}_k^j, N_k^j), \quad (13)$$

where SmoothL1 ($\text{beta} = 0.2$) is defined in Equation 12, N_k^j is the valid normal prior, \hat{N}_k^j is the rendered normal, and n is the number of rays that have a valid normal prior. This optimization term makes the surface normal in a texture-less region consistent with the normal prior. However, due to the noise in the priors, the lack of distance prior and inaccurate camera poses, the reconstructed texture-less surface may be unsmooth and even appear to have severe discontinuity caused by shape-radiance ambiguity. Therefore, we propose perturbation-residual restrictions to improve the reconstruction quality.

4.3 Perturbation-residual Restrictions

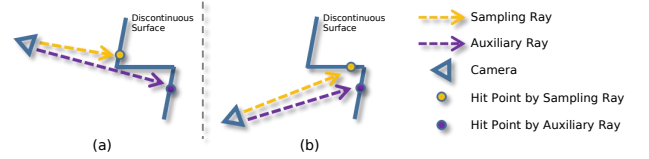


Fig. 6. Two cases illustrating perturbation-residual restriction. The surface should be continuous but break in the cases. In case (a), the two hit points are far from each other with the same surface normal. Thus, $\mathcal{L}_{consist_N}$ is small, and \mathcal{L}_{smooth_D} is large. In case (b), the two hit points are near each other, but the surface normal is quite different, which leads to a small \mathcal{L}_{smooth_D} and a large $\mathcal{L}_{consist_N}$. Only when the local surface is smooth, the two losses will be small at the same time.

Although we use two priors to guide the optimization, still we face some problems. One is that the depth and normal estimation results always have noise. Another is that the normal estimation of a region may be inconsistent. The inaccurate camera pose, unstable light condition and poor photo imaging quality easily cause the above situation.

The derivative of geometric network f at the sample point is the normal of that position. The normal obtained by this computing method is a very local constraint. Because the sampling ray is discrete and random, the normal condition can only ensure that the normal corresponding to the sampling ray is consistent with the prior and cannot affect a larger neighborhood. The rendered color loss cannot play an effective role in the texture-less region, and the distance prior generally cannot be obtained by MVS. At the same time, the normal prior can not uniquely determine a spatial location, resulting in the optimized surface geometry fluctuating and even breaking into many parts.

A natural solution, which may be the best, is to render the depth and normal of all rays in a patch from the net f to give geometric constraints. However, each sampling ray needs to query the network hundreds of times to obtain the data required for rendering. Moreover, rendering everything in a patch will consume considerable memory and computing time. Therefore, we propose a compromise approach called perturbation-residual restriction to establish connections between sampling rays, making the reconstructed surface continuous.

The perturbation-residual restrictions assume that in a small region, the sampling points should have the same normal, and the

distances to the camera center should be similar. We divide each optimization step into two stages. In the first stage, we randomly sample k rays as before and render their color \hat{C} , depth \hat{D} and normal \hat{N} . In the next stage, we perturb the ray direction. With the new sampling ray $P = \{o_k, v_k^{pert}\}$, we query the net f again and render the corresponding depth \hat{D}^{pert} and normal \hat{N}^{pert} . Then the residual is calculated with the first stage. The ray direction corresponding to a pixel $p_k : (u, v) \in I_i$ in the world coordinate is

$$v_k = R_i^{-1} \text{Normalize}(K_i^{-1} \begin{pmatrix} u \\ v \\ 1 \end{pmatrix}), \quad (14)$$

$$v_k^{pert} = R_i^{-1} \text{Normalize}(K_i^{-1} \begin{pmatrix} u + (a - 0.5) * w \\ v + (b - 0.5) * w \\ 1 \end{pmatrix}), \quad (15)$$

where K_i is the intrinsic matrix of I_i , R_i is the rotation matrix belonging to the extrinsic matrix T_i , Normalize is the normalization function that normalizes the length of the vector to be 1, random variables $a, b \sim U[0, 1]$ obey the uniform distribution on $[0, 1]$, and w is a hyperparameter indicating the amplitude of perturbation. The perturbation-residual restrictions establish the connection between surrounding rays to share their geometric information. Then, we calculate the residual with the previous stage:

$$\mathcal{L}_{res} = \delta \mathcal{L}_{smooth_D} + \epsilon \mathcal{L}_{consist_N}, \quad (16)$$

$$\mathcal{L}_{smooth_D} = \frac{1}{k} \sum_k \text{SmoothL1}(\hat{D}_k, \hat{D}_k^{pert}), \quad (17)$$

$$\mathcal{L}_{consist_N} = \frac{1}{N_{prior_N}} \sum_k \text{SmoothL1}(N_k, \hat{N}_k^{pert}), \quad (18)$$

where SmoothL1 is the smooth L1 loss ($\beta = 0.1$) defined in Equation 12, N_{prior_N} is the number of valid N_k , δ and ϵ are two hyperparameters. \mathcal{L}_{smooth_D} is a smoothing term. This term works on all sampling rays, aiming to make the depth of the sampling ray and the corresponding perturbation ray close. If N_i has a valid value, then \hat{N}_k^{pert} would be constrained by $\mathcal{L}_{consist_N}$. These two optimization terms make the surface geometry in the flat region continuous and obey the normal prior.

The final loss function is defined as

$$\mathcal{L} = \mathcal{L}_{color} + \mathcal{L}_{prior} + \mathcal{L}_{res} + \mathcal{L}_{Eikonal}. \quad (19)$$

$$\mathcal{L}_{Eikonal} = \frac{1}{nk} \sum_{n,k} (|\nabla f(x_{n,k})| - 1)^2, \quad (20)$$

where $\mathcal{L}_{Eikonal}$ is the Eikonal term on the sampling points to regularize the SDF.

4.4 Mesh Extraction

For each spatial position in the optimization area, we query the geometry function f to obtain the corresponding TSDF value. Then, we use marching cube [Lorensen and Cline 1987] to extract the raw mesh. There are many positions we do not need in the raw mesh, so we conduct ray-tracing to obtain the depth map for each pose and perform TSDF fusion [Curless and Levoy 1996; Newcombe et al. 2011] to generate our final mesh model. Ray-tracing and TSDF fusion are implemented based on Open3D [Zhou et al. 2018].

5 EXPERIMENT

5.1 Experimental Setup

Dataset. We evaluate our approach and baseline methods on the indoor dataset, ScanNet (V2) [Dai et al. 2017]. We randomly select 8 test scenes from the intersection of the test set of Framenet [Huang et al. 2019] and ScanNet [Dai et al. 2017]. The [Bae et al. 2021] network has been pretrained on the training set of [Huang et al. 2019] for evaluation. We take one photo out of approximately every ten adjacent photos with an image resolution of 1296×968 .

Implementation Details. The geometry function f is modeled by an MLP, which consists of 8 hidden layers with a hidden size of 256. The color function c is modeled by an MLP, which consists of 4 hidden layers with a size of 256. Positional encoding, initialization of the implicit neural representation, and coarse to fine sampling methods are similar to the method of [Wang et al. 2021b]. The numbers of coarse and fine sampling points for each ray are 64 and 64, respectively. We sample 512 rays per batch and train NeuralRoom for 200k iterations on a single NVIDIA RTX2080Ti GPU. The hyperparameters used in the experiment are as follows: $e = 1.3$, $w = 2.4$, $\gamma = 0.001$, $\delta = 0.001$, and $\epsilon = 0.001$.

Baselines. We do not compare our method with rendering-based reconstruction methods [Oechsle et al. 2021; Wang et al. 2021b; Yariv et al. 2021] since these reconstruction methods often fails. We compare our method with the following baseline methods, NeuralRecon [Sun et al. 2021a] and Atlas [Murez et al. 2020], two volumetric multiview indoor scene reconstruction methods that directly extract 3D surface from feature volume; COLMAP [Schonberger and Frahm 2016] and ACMP [Xu and Tao 2020b], two traditional PatchMatch-based MVS methods; 3DVNet [Rich et al. 2021], a learning-based multiview stereo method that combines the advantages of depth-based and volumetric multiview stereo approaches; and ESTDepth [Long et al. 2021b], a learning-based multiview depth estimation method.

Evaluation Protocols. We choose a mesh as the 3D geometry representation for qualitative comparison and quantitative evaluation. For COLMAP, we perform Delaunay triangulation to form a mesh from a point cloud. For our method, Atlas, NeuralRecon and COLMAP with Delaunay triangulation, in which there are a large number of nonobservation areas. Therefore, we use ray tracing provided by Open3D [Zhou et al. 2018] on the reconstructed model to obtain the depth map of each view. Then we use TSDF fusion [Curless and Levoy 1996; Newcombe et al. 2011] to obtain a trimmed 3D mesh. For ACMP, ESTDepth and 3DVNet, we use TSDF fusion to obtain a mesh. The voxel length is $0.02m$, and the SDF truncation value is $0.12m$. For quantitative evaluation, we use a regular voxel grid to create a uniformly downsampled point cloud from the input mesh. The side length of the voxel grid is $0.005m$. The threshold of precision and recall is $0.05m$.

5.2 Geometry Prior Statistics

We perform the quantitative evaluation for the prior on all test scenes. The distance prior is converted from the corresponding MVS depth map, so we evaluate the depth map instead. The depth map



Fig. 7. Visualization results on ScanNet. We compared our reconstruction results with those of COLMAP [Schonberger and Frahm 2016] and other advanced learning-based indoor scene reconstruction methods [Long et al. 2021b; Murez et al. 2020; Rich et al. 2021; Sun et al. 2021a]. The reconstruction results of NeuralRoom exhibit similar scene integrity in visual perception to those of Atlas. The details are preserved better than other algorithms. The quantitative evaluation is shown in Table 3.

and normal map are evaluated in Table 1 and Table 2. The evaluation of the normal map filtered by uncertainty has a `_50` extension. After filtering, we obtain highly accurate normal estimation results, for which the mean angle error is 8.183° .

Table 1. Quantitative evaluation of the depth map acquired by COLMAP.

Comp	Abs Diff	Abs Rel	Sq Rel	RMSE
0.143	0.093	0.042	0.013	0.158

Table 2. Quantitative evaluation of the acquired normal map. The filtered normal maps are with a `_50` extension.

Mean	Median	RMSE	Mean_50	Median_50	RMSE_50
14.691	7.329	23.224	8.183	4.931	13.030

5.3 Evaluation Results

We provide qualitative and quantitative comparisons on the ScanNet dataset to evaluate the performance of our system. Our method achieves state-of-the-art both quantitatively and qualitatively. Since

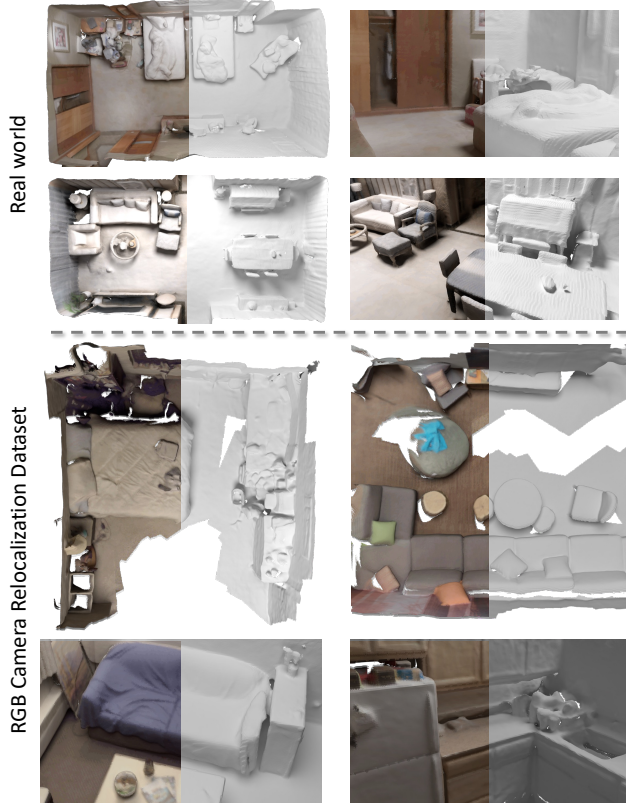


Fig. 8. We applied NeuralRoom to real-world scenes and RGB Camera Relocalization Dataset [Valentin et al. 2016].

all algorithms will produce some additional reconstruction areas, for a fair comparison, we perform ray tracing with ground truth camera parameters to get the corresponding depth, and then perform TSDF fusion to acquire cleaned 3D reconstruction.

Visual comparison. Figure 7 shows our full scene and detailed visualization results compared with those of different reconstruction methods, including COLMAP [Schonberger and Frahm 2016], Atlas [Murez et al. 2020], NeuralRecon [Sun et al. 2021a], 3DVNet [Rich et al. 2021], ESTDepth [Long et al. 2021b] and ground truth [Dai et al. 2017].

COLMAP [Schonberger and Frahm 2016] produces accurate geometry in rich textured areas, but it cannot handle texture-less areas. The details are preserved to some extent. The cross-view consistency of the ESTDepth [Long et al. 2021b] is not good, so the reconstruction results are not ideal. Atlas [Murez et al. 2020] and NeuralRecon [Sun et al. 2021a] are end-to-end 3D reconstruction methods that directly regress a TSDF from calibrated images. Atlas usually obtains a coarse but continuous reconstruction. The details of the scene are difficult to reconstruct by Atlas. The NeuralRecon can obtain better details but sacrifice completeness. 3DVNet [Rich et al. 2021] is a learning-based multiview stereo method, it can produce better visual effects than other algorithms. However, the

output depth map resolution of 3DVNet is low, which results in the reconstruction results with less precise details.

Compared with other algorithms, our reconstruction results have higher reconstruction integrity and finer details. The visual effect of some reconstructed areas is better than that of the ground truth. In addition, we tested our algorithm on real-world scenes and RGB Camera Relocalization Dataset [Valentin et al. 2016], Figure 8 shows the reconstruction results. We use mobile phones to take high-resolution photos of two real-world scenes. The resolution of photos is 4608×3456 . First, we use COLMAP [Schonberger and Frahm 2016] to calculate camera parameters, obtain dense depth maps and define the bounding box. Next, we resize images and depth maps to 1296×968 , then feed the images to the normal estimation network [Bae et al. 2021] to obtain the normal prior. The normal estimation network was only pretrained on the ScanNet [Dai et al. 2017] dataset without fine-tuning. The camera intrinsics are different from ScanNet, which may influence the accuracy of the normal estimation. Finally, we use NeuralRoom to reconstruct the scene. The results show our algorithm’s robustness.

Quantitative comparison. Table 3 reports the summary of 3D geometry metrics for different methods. COLMAP [Schonberger and Frahm 2016] and ACMP [Xu and Tao 2020b] are traditional MVS methods, ESTDepth [Long et al. 2021b] is a multiview depth estimation method, 3DVNet [Rich et al. 2021] is a learning-based multiview stereo method, Atlas [Murez et al. 2020] and NeuralRecon [Sun et al. 2021a] are learning-based reconstruction methods. Since rendering-based reconstruction methods have a high probability that the satisfactory reconstruction of indoor scenes cannot be acquired through input images (Figure 2), we only evaluate the methods mentioned above.

The ACMP reconstructs the indoor scene with the plane hypothesis. The reconstruction always has many outliers, resulting in low accuracy and precision scores. Our method has a relatively balanced performance in accuracy and completeness. The overall performance is much better than that of other different types of methods. We believe that the improvements come from the following aspects:

Table 3. Quantitative evaluation of reconstruction with existing methods on the ScanNet dataset. We report the average results for eight scenes from the test set.

Method	Prec \uparrow	Recall \uparrow	F-score \uparrow	Acc \downarrow	Comp \downarrow	Overall \downarrow
COLMAP	45.136	44.510	44.678	0.108	0.136	0.122
ACMP	35.978	<u>70.691</u>	47.622	0.152	<u>0.047</u>	0.100
ESTDepth	38.217	50.992	43.589	0.144	0.075	0.110
3DVNet	64.961	64.562	64.665	0.071	0.061	0.066
Atlas	67.957	57.747	61.871	<u>0.050</u>	0.090	0.070
NeuralRecon	63.851	47.401	54.208	0.054	0.128	0.091
Ours	<u>68.347</u>	65.298	<u>66.756</u>	0.051	0.058	<u>0.055</u>

Distance prior. The distance prior guides the implicit surface close to the corresponding point, which gives the NeuralRoom the ability to preserve the reliable spatial information. The weight of the

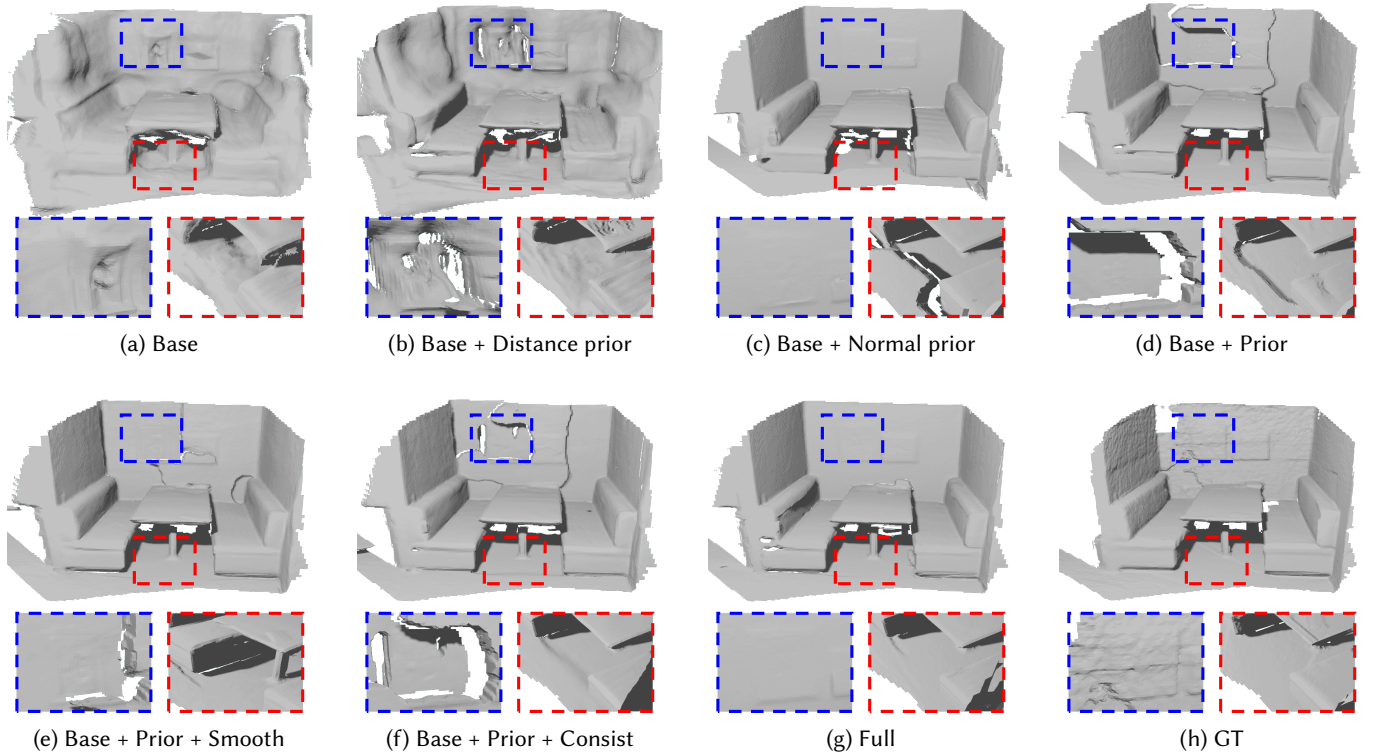


Fig. 9. Visualization results of the ablation study of a simple scene without a boundingbox. The analysis is presented in Section 5.4. The quantitative comparisons are shown in Table 4.

distance prior loss in optimization can be adjusted according to its quality.

Normal prior. The normal prior is the most important prior. With a normal prior, NeuralRoom can make the surface normal of the texture-less region consistent. This leads to better visual effects and quantitative evaluation. The weight of the normal prior loss in optimization can also be adjusted according to its quality.

Perturbation-residual restrictions. The perturbation-residual restrictions ensure the continuity of the reconstructed scene and improve the accuracy and completeness. It establishes a connection between the sampling ray and the corresponding auxiliary ray.

Differentiable renderer. The key to combining the above three aspects is our NeuralRoom differentiable renderer. The reliable priors reduce the possible spatial variation range of an implicit neural surface which helps the NeuralRoom alleviate shape-radiance ambiguity. The renderer takes the color loss as a primary loss to optimize an implicit neural surface that can render an image consistent with the input training images. In addition, the renderer has the ability to resist the influence caused by incorrect geometric priors. Similar to volumetric methods [Murez et al. 2020; Sun et al. 2021a], the renderer considers the influence of all inputs in the reconstruction optimization, while the depth estimation method usually only considers the neighborhood.

5.4 Ablation Study

To better understand the role of each optimization item, we performed ablation studies over each component of the proposed system. The experiment was conducted on Scene0801_00 in ScanNet. Some simple scenes like that can be reconstructed without a bounding box and are sensitive to each loss term. The qualitative evaluation is shown in Figure 9, and the quantitative evaluation is shown in Table 4. In addition, we also perform an ablation study on the complex real-world scene.

Table 4. Ablation study of a simple scene without a boundingbox. Some scenes with simple geometry can be reconstructed without boundingbox like Scene0801_00. We test the effect of each loss function in the method. This analysis shows that our full method performs best both visually and quantitatively.

	Method	Comp↓	Acc↓	Overall↓
a	Base	0.055	0.157	0.106
b	Base + Distance prior	0.048	0.095	0.072
c	Base + Normal prior	0.050	0.059	0.054
d	Base + Prior	0.031	0.050	0.041
e	Base + Prior + Smooth	0.033	0.054	0.044
f	Base + Prior + Consist	0.027	0.041	0.034
g	Full	<u>0.022</u>	<u>0.027</u>	<u>0.024</u>

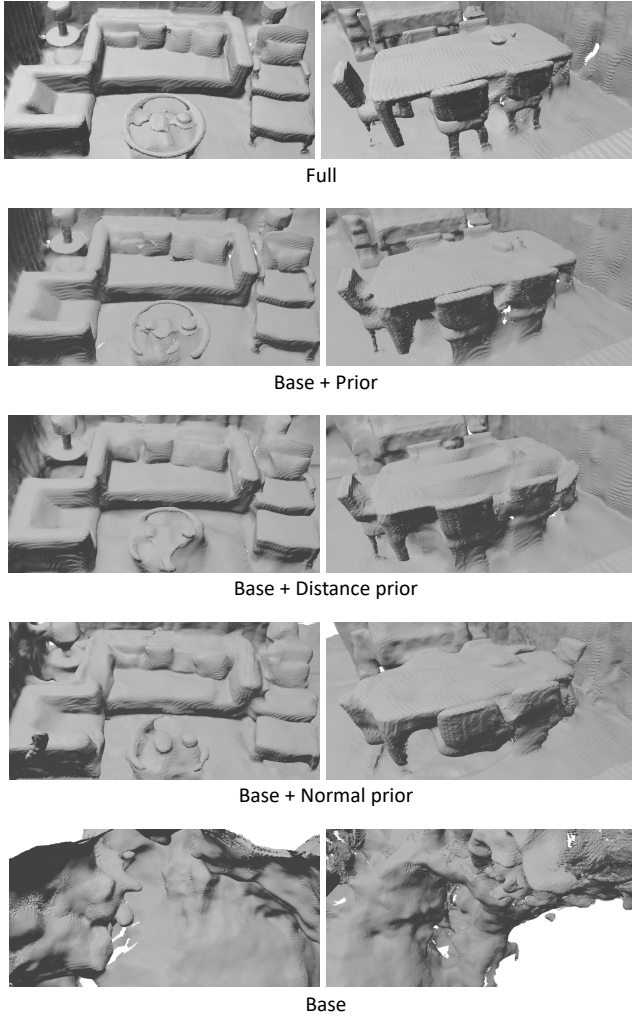


Fig. 10. Visualization results of the ablation study on a real-world scene.

The distance prior \mathcal{L}_{prior_D} provides accurate 3D points, which helps improve the accuracy of the reconstruction. The rich textured and edge areas are well reconstructed. The normal prior \mathcal{L}_{prior_N} is the most important term of our system, which can significantly improve the completeness and accuracy of the scene. When both \mathcal{L}_{prior_D} and \mathcal{L}_{prior_N} participate in optimization at the same time, the accuracy and completeness of reconstruction are further improved. There are cracks in texture-less areas, although the quantitative results are better than before. The noise that exists in the priors and the lack of distance prior may cause this phenomenon. The residual-perturbation restrictions \mathcal{L}_{smooth_D} and $\mathcal{L}_{consist_N}$ establish a connection between the sampling ray and its corresponding auxiliary ray, which improves the reconstruction quality of the surface. Using $\mathcal{L}_{consist_N}$ alone can improve the completeness and accuracy, but more cracks appear in the scene. The normal of two points far apart in space can also be consistent, so only considering the normal constraint cannot determine a unique position in space.

The \mathcal{L}_{smooth_D} term is used to limit the spatial distance between two points, which is designed to smooth the scene. When both local normal and smooth constraints are added to the optimization, we can obtain a better visual effect and quantitative evaluation result. In addition, we can adjust the corresponding weight according to the quality of the prior, so as to obtain a better reconstruction result.

5.5 Computational cost

When the layer number of Geo-MLP and Color-MLP are 8 and 4 respectively, and the number of sampling rays is 64+64, the GPU memory consumption is 9615M, and the time consumption is 16h on a single RTX 2080Ti. Without the perturbation-residual restriction, time and memory usage drop by about a quarter. When the number of sampling rays is reduced to 32+32, it takes 5353M and 10h. The reconstruction result will lose a little detail, but the overall reconstruction quality is OK. When the layers of Geo-MLP and Color-MLP are further reduced to 4 and 2 respectively, it takes 3405M and 7h. This setting is OK for reconstructing the scenes in the teaser and ablation study, but the capacity of MLP (4+2) is not enough for reconstructing some more complex scenes shown in Fig7. We believe that if the MLP is replaced with more advanced parameter representations like InstantNGP [Müller et al. 2022] and TensoRF [Chen et al. 2022], the running speed can be increased significantly.

5.6 Advantages and Limitation

The depth sensor emitting infrared rays has difficulty to collect the depth information of the mirror, black area and distant objects, which results in incomplete reconstruction. NeuralRoom takes RGB images as input, which can restore this part of the scene (Figure 11 left). However, there are several limitations of the proposed method.

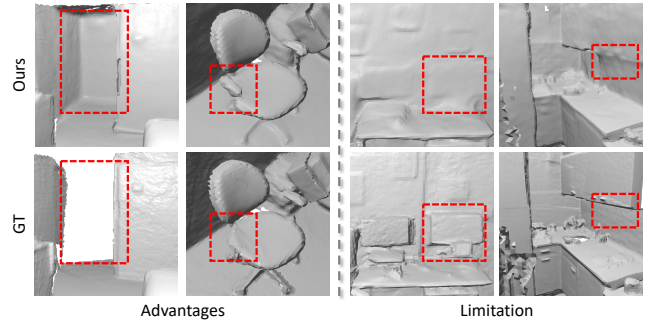


Fig. 11. Advantages and limitations.

Poses and priors. Almost all rendering-based reconstruction methods rely on the accurate camera pose. Therefore, large poses and priors errors have a strong adverse impact on reconstruction results. In addition, when the two surfaces with the same normal are close to each other, if the correct distance prior is missing, the NeuralRoom will over smooth them (Figure 11, right). Using more advanced learning-based pose, depth and normal estimation methods to provide more reliable geometry priors and camera poses can ensure the reconstruction quality.

Computational cost. Our method requires a large amount of computational resources for geometry prior computation and renderer training. Accelerating with an updated differentiable rendering [Müller et al. 2022; Yu et al. 2021] architecture is a direction for improvement. Moreover, using a neural network such as [Murez et al. 2020] to quickly reconstruct a structure of the scene and then using a differentiable renderer or other learning-based methods to adjust the details of the indoor scene may be a good solution.

5.7 NeuralRoom-Advanced

We use more advanced indoor scene reconstruction algorithms [Murez et al. 2020; Rich et al. 2021; Sun et al. 2021a] instead of COLMAP [Schonberger and Frahm 2016] to provide distance priors, and show the improved reconstruction quality of these algorithms achieved by our proposed NeuralRoom system.

Table 5. Quantitative evaluation illustrating the improvement of existing reconstruction algorithms achieved by our proposed NeuralRoom system.

Method	Prec \uparrow	Recall \uparrow	F-score \uparrow	Acc \downarrow	Comp \downarrow	Overall \downarrow
NeuralRoom	68.347	65.298	66.756	0.051	0.058	0.055
NR-Atlas	73.003	69.062	70.948	<u>0.044</u>	0.052	<u>0.048</u>
NR-NeuralRecon	69.977	66.965	68.393	0.054	0.059	0.056
NR-3DVNet	<u>73.339</u>	<u>70.496</u>	<u>71.865</u>	0.046	<u>0.051</u>	<u>0.048</u>

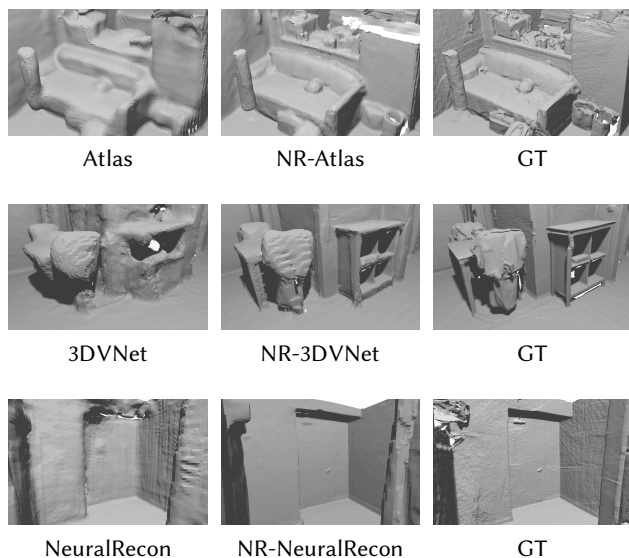


Fig. 12. The improvement of reconstruction quality of different reconstruction algorithms by our proposed NeuralRoom system.

These learning-based multiview reconstruction algorithms provide a distance prior with higher accuracy or better completeness than COLMAP [Schonberger and Frahm 2016], which will help further alleviate shape-radiance ambiguity resulting in better reconstructions. Table 5 shows the quantitative evaluation and Figure 12 shows the qualitative comparisons, the related algorithms improved

by NeuralRoom have an NR- prefix. In addition to replacing the distance prior module in NeuralRoom, researchers can further improve the reconstruction quality by replacing the normal estimation module and differentiable renderer with their own more advanced algorithms.

6 CONCLUSIONS

We present NeuralRoom, a rendering-based neural surface reconstruction method for reconstructing indoor scenes directly from a set of 2D images. The key to successful indoor scene reconstruction by using differentiable rendering is that we find complementarity between depth estimation and normal estimation methods, which helps alleviate inherent shape-radiance ambiguity. We also design geometric constraints for the renderer to obtain a more smoothing and complete surface reconstruction. NeuralRoom produces impressive reconstruction and successfully reconstructs the surface with no texture or rich texture. In addition, we show the reconstruction improvement of existing multiview reconstruction algorithms by incorporating NeuralRoom pipeline.

ACKNOWLEDGMENTS

This work is partially supported by NSFC (No. 61972298) and Wuhan University-Huawei GeoInformatics Innovation Lab.

REFERENCES

- Matan Atzmon, Niv Haim, Lior Yariv, Ofer Israelov, Haggai Maron, and Yaron Lipman. 2019. Controlling neural level sets. *Advances in Neural Information Processing Systems* 32 (2019).
- Matan Atzmon and Yaron Lipman. 2020. Sal: Sign agnostic learning of shapes from raw data. In *Proceedings of the IEEE/CVF Conference on Computer Vision and Pattern Recognition*. 2565–2574.
- Gwangbin Bae, Ignas Budvytis, and Roberto Cipolla. 2021. Estimating and Exploiting the Aleatoric Uncertainty in Surface Normal Estimation. In *Proceedings of the IEEE/CVF International Conference on Computer Vision*. 13137–13146.
- Jonathan T Barron, Ben Mildenhall, Matthew Tancik, Peter Hedman, Ricardo Martin-Brualla, and Pratul P Srinivasan. 2021. Mip-nerf: A multiscale representation for anti-aliasing neural radiance fields. In *Proceedings of the IEEE/CVF International Conference on Computer Vision*. 5855–5864.
- Fausto Bernardini, Joshua Mittleman, Holly Rushmeier, Cláudio Silva, and Gabriel Taubin. 1999. The ball-pivoting algorithm for surface reconstruction. *IEEE transactions on visualization and computer graphics* 5, 4 (1999), 349–359.
- Alexey Bokhovkin and Angela Dai. 2022. Neural Part Priors: Learning to Optimize Part-Based Object Completion in RGB-D Scans. *arXiv preprint arXiv:2203.09375* (2022).
- Chris Buehler, Michael Bosse, Leonard McMillan, Steven Gortler, and Michael Cohen. 2001. Unstructured lumigraph rendering. In *Proceedings of the 28th annual conference on Computer graphics and interactive techniques*. 425–432.
- Jin-Xiang Chai, Xin Tong, Shing-Chow Chan, and Heung-Yeung Shum. 2000. Plenoptic sampling. In *Proceedings of the 27th annual conference on Computer graphics and interactive techniques*. 307–318.
- Anpei Chen, Zexiang Xu, Andreas Geiger, Jingyi Yu, and Hao Su. 2022. TensorRF: Tensorial Radiance Fields. *arXiv preprint arXiv:2203.09517* (2022).
- Anpei Chen, Zexiang Xu, Fuqiang Zhao, Xiaoshuai Zhang, Fanbo Xiang, Jingyi Yu, and Hao Su. 2021. Mvsnerf: Fast generalizable radiance field reconstruction from multiview stereo. In *Proceedings of the IEEE/CVF International Conference on Computer Vision*. 14124–14133.
- Rui Chen, Songfang Han, Jing Xu, and Hao Su. 2019. Point-based multi-view stereo network. In *Proceedings of the IEEE/CVF International Conference on Computer Vision*. 1538–1547.
- Shuo Cheng, Zexiang Xu, Shilin Zhu, Zhuwen Li, Li Erran Li, Ravi Ramamoorthi, and Hao Su. 2020. Deep stereo using adaptive thin volume representation with uncertainty awareness. In *Proceedings of the IEEE/CVF Conference on Computer Vision and Pattern Recognition*. 2524–2534.
- Christopher B Choy, Danfei Xu, JunYoung Gwak, Kevin Chen, and Silvio Savarese. 2016. 3d-r2n2: A unified approach for single and multi-view 3d object reconstruction. In *European conference on computer vision*. Springer, 628–644.

- Robert T Collins. 1996. A space-sweep approach to true multi-image matching. In *Proceedings CVPR IEEE Computer Society Conference on Computer Vision and Pattern Recognition*. IEEE, 358–363.
- Brian Curless and Marc Levoy. 1996. A volumetric method for building complex models from range images. In *Proceedings of the 23rd annual conference on Computer graphics and interactive techniques*. 303–312.
- Angela Dai, Angel X. Chang, Manolis Savva, Maciej Halber, Thomas Funkhouser, and Matthias Nießner. 2017. ScanNet: Richly-annotated 3D Reconstructions of Indoor Scenes. In *Proc. Computer Vision and Pattern Recognition (CVPR), IEEE*.
- Angela Dai, Christian Diller, and Matthias Nießner. 2020. Sg-nn: Sparse generative neural networks for self-supervised scene completion of rgb-d scans. In *Proceedings of the IEEE/CVF Conference on Computer Vision and Pattern Recognition*. 849–858.
- Angela Dai, Yawar Siddiqui, Justus Thies, Julien Valentin, and Matthias Nießner. 2021. Spsg: Self-supervised photometric scene generation from rgb-d scans. In *Proceedings of the IEEE/CVF Conference on Computer Vision and Pattern Recognition*. 1747–1756.
- Paul E Debevec, Camillo J Taylor, and Jitendra Malik. 1996. Modeling and rendering architecture from photographs: A hybrid geometry-and image-based approach. In *Proceedings of the 23rd annual conference on Computer graphics and interactive techniques*. 11–20.
- Yikang Ding, Wentao Yuan, Qingtian Zhu, Haotian Zhang, Xiangyue Liu, Yuanjiang Wang, and Xiao Liu. 2021. TransMVSNet: Global Context-aware Multi-view Stereo Network with Transformers. *arXiv preprint arXiv:2111.14600* (2021).
- Tien Do, Khiem Vuong, Stergios I Roumeliotis, and Hyun Soo Park. 2020. Surface normal estimation of tilted images via spatial rectifier. In *European Conference on Computer Vision*. Springer, 265–280.
- Silvano Galliani, Katrin Lasinger, and Konrad Schindler. 2015. Massively parallel multi-view stereopsis by surface normal diffusion. In *Proceedings of the IEEE International Conference on Computer Vision*. 873–881.
- Kyle Genova, Forrester Cole, Daniel Vlasic, Aaron Sarna, William T Freeman, and Thomas Funkhouser. 2019. Learning shape templates with structured implicit functions. In *Proceedings of the IEEE/CVF International Conference on Computer Vision*. 7154–7164.
- Xiaodong Gu, Zhiwen Fan, Siyu Zhu, Zuozhuo Dai, Feitong Tan, and Ping Tan. 2020. Cascade cost volume for high-resolution multi-view stereo and stereo matching. In *Proceedings of the IEEE/CVF Conference on Computer Vision and Pattern Recognition*. 2495–2504.
- Haoyu Guo, Sida Peng, Haotong Lin, Qianqian Wang, Guofeng Zhang, Hujun Bao, and Xiaowei Zhou. 2022. Neural 3D Scene Reconstruction with the Manhattan-world Assumption. In *Proceedings of the IEEE/CVF Conference on Computer Vision and Pattern Recognition*. 5511–5520.
- Yuxin Hou, Juho Kannala, and Arno Solin. 2019. Multi-view stereo by temporal nonparametric fusion. In *Proceedings of the IEEE/CVF International Conference on Computer Vision*. 2651–2660.
- Jingwei Huang, Yichao Zhou, Thomas Funkhouser, and Leonidas J Guibas. 2019. Framenet: Learning local canonical frames of 3d surfaces from a single rgb image. In *Proceedings of the IEEE/CVF International Conference on Computer Vision*. 8638–8647.
- Mengqi Ji, Juergen Gall, Haitian Zheng, Yebin Liu, and Lu Fang. 2017. SurfacerNet: An end-to-end 3d neural network for multiview stereopsis. In *Proceedings of the IEEE International Conference on Computer Vision*. 2307–2315.
- Mengqi Ji, Jinzhi Zhang, Qionghai Dai, and Lu Fang. 2020. SurfaceNet+: An end-to-end 3D neural network for very sparse multi-view stereopsis. *IEEE Transactions on Pattern Analysis and Machine Intelligence* 43, 11 (2020), 4078–4093.
- Hualie Jiang, Laiyan Ding, Junjie Hu, and Rui Huang. 2021. PLNet: Plane and Line Priors for Unsupervised Indoor Depth Estimation. In *2021 International Conference on 3D Vision (3DV)*. IEEE, 741–750.
- Abhishek Kar, Christian Häne, and Jitendra Malik. 2017. Learning a multi-view stereo machine. *Advances in neural information processing systems* 30 (2017).
- Michael Kazhdan, Matthew Bolitho, and Hugues Hoppe. 2006. Poisson surface reconstruction. In *Proceedings of the fourth Eurographics symposium on Geometry processing*, Vol. 7.
- Petr Kellnhofer, Lars C Jebe, Andrew Jones, Ryan Spicer, Kari Pulli, and Gordon Wetstein. 2021. Neural lumigraph rendering. In *Proceedings of the IEEE/CVF Conference on Computer Vision and Pattern Recognition*. 4287–4297.
- Andreas Kuhn, Christian Sormann, Mattia Rossi, Oliver Erdler, and Friedrich Fraundorfer. 2020. Deepc-mvs: Deep confidence prediction for multi-view stereo reconstruction. In *2020 International Conference on 3D Vision (3DV)*. IEEE, 404–413.
- Jie Liao, Yanping Fu, Qingan Yan, Fei Luo, and Chunxia Xiao. 2021. Adaptive depth estimation for pyramid multi-view stereo. *Computers & Graphics* 97 (2021), 268–278.
- Hongmin Liu, Kincheng Tang, and Shuhan Shen. 2020b. Depth-map completion for large indoor scene reconstruction. *Pattern Recognition* 99 (2020), 107112.
- Lingjie Liu, Jiatao Gu, Kyaw Zaw Lin, Tat-Seng Chua, and Christian Theobalt. 2020a. Neural sparse voxel fields. *Advances in Neural Information Processing Systems* 33 (2020), 15651–15663.
- Xiaoxiao Long, Cheng Lin, Lingjie Liu, Wei Li, Christian Theobalt, Ruigang Yang, and Wenping Wang. 2021a. Adaptive surface normal constraint for depth estimation. In *Proceedings of the IEEE/CVF International Conference on Computer Vision*. 12849–12858.
- Xiaoxiao Long, Lingjie Liu, Wei Li, Christian Theobalt, and Wenping Wang. 2021b. Multi-view depth estimation using epipolar spatio-temporal networks. In *Proceedings of the IEEE/CVF Conference on Computer Vision and Pattern Recognition*. 8258–8267.
- William E Lorensen and Harvey E Cline. 1987. Marching cubes: A high resolution 3D surface construction algorithm. *ACM siggraph computer graphics* 21, 4 (1987), 163–169.
- Paul Merrell, Amir Akbarzadeh, Liang Wang, Philippos Mordohai, Jan-Michael Frahm, Ruigang Yang, David Nistér, and Marc Pollefeys. 2007. Real-time visibility-based fusion of depth maps. In *2007 IEEE 11th International Conference on Computer Vision*. IEEE, 1–8.
- Lars Mescheder, Michael Oechsle, Michael Niemeyer, Sebastian Nowozin, and Andreas Geiger. 2019. Occupancy networks: Learning 3d reconstruction in function space. In *Proceedings of the IEEE/CVF Conference on Computer Vision and Pattern Recognition*. 4460–4470.
- Mateusz Michalkiewicz, Jhony K Pontes, Dominic Jack, Mahsa Baktashmotlagh, and Anders Eriksson. 2019. Implicit surface representations as layers in neural networks. In *Proceedings of the IEEE/CVF International Conference on Computer Vision*. 4743–4752.
- Ben Mildenhall, Pratul P Srinivasan, Matthew Tancik, Jonathan T Barron, Ravi Ramamoorthi, and Ren Ng. 2020. Nerf: Representing scenes as neural radiance fields for view synthesis. In *European conference on computer vision*. Springer, 405–421.
- Thomas Müller, Alex Evans, Christoph Schied, and Alexander Keller. 2022. Instant Neural Graphics Primitives with a Multiresolution Hash Encoding. *arXiv preprint arXiv:2201.05989* (2022).
- Zak Murez, Tarrence van As, James Bartolozzi, Ayan Sinha, Vijay Badrinarayanan, and Andrew Rabinovich. 2020. Atlas: End-to-end 3d scene reconstruction from posed images. In *European Conference on Computer Vision*. Springer, 414–431.
- Richard A Newcombe, Shahram Izadi, Otmar Hilliges, David Molyneaux, David Kim, Andrew J Davison, Pushmeet Kohi, Jamie Shotton, Steve Hodges, and Andrew Fitzgibbon. 2011. Kinectfusion: Real-time dense surface mapping and tracking. In *2011 10th IEEE international symposium on mixed and augmented reality*. IEEE, 127–136.
- Michael Niemeyer, Jonathan T Barron, Ben Mildenhall, Mehdi SM Sajjadi, Andreas Geiger, and Noha Radwan. 2021. RegNeRF: Regularizing Neural Radiance Fields for View Synthesis from Sparse Inputs. *arXiv preprint arXiv:2112.00724* (2021).
- Michael Niemeyer, Lars Mescheder, Michael Oechsle, and Andreas Geiger. 2020. Differentiable volumetric rendering: Learning implicit 3d representations without 3d supervision. In *Proceedings of the IEEE/CVF Conference on Computer Vision and Pattern Recognition*. 3504–3515.
- Michael Oechsle, Songyou Peng, and Andreas Geiger. 2021. Unisurf: Unifying neural implicit surfaces and radiance fields for multi-view reconstruction. In *Proceedings of the IEEE/CVF International Conference on Computer Vision*. 5589–5599.
- Jeong Joon Park, Peter Florence, Julian Straub, Richard Newcombe, and Steven Lovegrove. 2019. DeepSDF: Learning continuous signed distance functions for shape representation. In *Proceedings of the IEEE/CVF Conference on Computer Vision and Pattern Recognition*. 165–174.
- A. Paszke, S. Gross, F. Massa, A. Lerer, and S. Chintala. 2019. PyTorch: An Imperative Style, High-Performance Deep Learning Library.
- Songyou Peng, Michael Niemeyer, Lars Mescheder, Marc Pollefeys, and Andreas Geiger. 2020. Convolutional occupancy networks. In *European Conference on Computer Vision*. Springer, 523–540.
- Julien Philip, Sébastien Mordohai, Michaël Gharbi, and George Drettakis. 2021. Free-viewpoint indoor neural relighting from multi-view stereo. *ACM Transactions on Graphics (TOG)* 40, 5 (2021), 1–18.
- Alexander Rich, Noah Stier, Pradeep Sen, and Tobias Höllerer. 2021. 3DVNet: Multi-View Depth Prediction and Volumetric Refinement. In *2021 International Conference on 3D Vision (3DV)*. IEEE, 700–709.
- Barbara Roessle, Jonathan T Barron, Ben Mildenhall, Pratul P Srinivasan, and Matthias Nießner. 2021. Dense Depth Priors for Neural Radiance Fields from Sparse Input Views. *arXiv preprint arXiv:2112.03288* (2021).
- Shunsuke Saito, Zeng Huang, Ryota Natsume, Shiguo Morishima, Angjoo Kanazawa, and Hao Li. 2019. Pifu: Pixel-aligned implicit function for high-resolution clothed human digitization. In *Proceedings of the IEEE/CVF International Conference on Computer Vision*. 2304–2314.
- Shunsuke Saito, Tomas Simon, Jason Saragih, and Hanbyul Joo. 2020. Pifuhd: Multi-level pixel-aligned implicit function for high-resolution 3d human digitization. In *Proceedings of the IEEE/CVF Conference on Computer Vision and Pattern Recognition*. 84–93.
- Johannes L Schonberger and Jan-Michael Frahm. 2016. Structure-from-motion revisited. In *Proceedings of the IEEE conference on computer vision and pattern recognition*. 4104–4113.
- Steven M Seitz, Brian Curless, James Diebel, Daniel Scharstein, and Richard Szeliski. 2006. A comparison and evaluation of multi-view stereo reconstruction algorithms. In *2006 IEEE computer society conference on computer vision and pattern recognition*

- (CVPR'06), Vol. 1. IEEE, 519–528.
- Jiaming Sun, Yiming Xie, Linghao Chen, Xiaowei Zhou, and Hujun Bao. 2021a. Neural-Recon: Real-time coherent 3D reconstruction from monocular video. In *Proceedings of the IEEE/CVF Conference on Computer Vision and Pattern Recognition*. 15598–15607.
- Shang Sun, Yunan Zheng, Xuelei Shi, Zhenyu Xu, and Yiguang Liu. 2021b. PHI-MVS: Plane Hypothesis Inference Multi-view Stereo for Large-Scale Scene Reconstruction. *arXiv preprint arXiv:2104.06165* (2021).
- Matthew Tancik, Vincent Casser, Xinchen Yan, Sabeek Pradhan, Ben Mildenhall, Pratul P Srinivasan, Jonathan T Barron, and Henrik Kretzschmar. 2022. Block-NeRF: Scalable Large Scene Neural View Synthesis. *arXiv preprint arXiv:2202.05263* (2022).
- Zachary Teed and Jia Deng. 2018. Deepv2d: Video to depth with differentiable structure from motion. *arXiv preprint arXiv:1812.04605* (2018).
- Julien Valentin, Angela Dai, Matthias Nießner, Pushmeet Kohli, Philip Torr, Shahram Izadi, and Cem Keskin. 2016. Learning to Navigate the Energy Landscape. *arXiv preprint arXiv:1603.05772* (2016).
- Fangjunhua Wang, Silvano Galliani, Christoph Vogel, Pablo Speciale, and Marc Pollefeys. 2021a. Patchmatchnet: Learned multi-view patchmatch stereo. In *Proceedings of the IEEE/CVF Conference on Computer Vision and Pattern Recognition*. 14194–14203.
- Jiepeng Wang, Peng Wang, Xiaoxiao Long, Christian Theobalt, Taku Komura, Lingjie Liu, and Wenping Wang. 2022. NeuRIS: Neural Reconstruction of Indoor Scenes Using Normal Priors. *arXiv preprint arXiv:2206.13597* (2022).
- Kaixuan Wang and Shaojie Shen. 2018. Mvdepthnet: Real-time multiview depth estimation neural network. In *2018 International conference on 3d vision (3DV)*. IEEE, 248–257.
- Peng Wang, Lingjie Liu, Yuan Liu, Christian Theobalt, Taku Komura, and Wenping Wang. 2021b. Neus: Learning neural implicit surfaces by volume rendering for multi-view reconstruction. *arXiv preprint arXiv:2106.10689* (2021).
- Rui Wang, David Geraghty, Kevin Matzen, Richard Szeliski, and Jan-Michael Frahm. 2020. Vplnet: Deep single view normal estimation with vanishing points and lines. In *Proceedings of the IEEE/CVF Conference on Computer Vision and Pattern Recognition*. 689–698.
- Yi Wei, Shaohui Liu, Yongming Rao, Wang Zhao, Jiwen Lu, and Jie Zhou. 2021a. Nerf-gmvs: Guided optimization of neural radiance fields for indoor multi-view stereo. In *Proceedings of the IEEE/CVF International Conference on Computer Vision*. 5610–5619.
- Zizhuang Wei, Qingtian Zhu, Chen Min, Yisong Chen, and Guoping Wang. 2021b. Aarmvsnet: Adaptive aggregation recurrent multi-view stereo network. In *Proceedings of the IEEE/CVF International Conference on Computer Vision*. 6187–6196.
- Yuanbo Xiangli, Linning Xu, Xingang Pan, Nanxuan Zhao, Anyi Rao, Christian Theobalt, Bo Dai, and Dahua Lin. 2021. CityNeRF: Building NeRF at City Scale. *arXiv preprint arXiv:2112.05504* (2021).
- Hongbin Xu, Zhipeng Zhou, Yu Qiao, Wenxiong Kang, and Qiuxia Wu. 2021. Self-supervised multi-view stereo via effective co-segmentation and data-augmentation. In *Proceedings of the AAAI Conference on Artificial Intelligence*, Vol. 2. 6.
- Jiamin Xu, Zihan Zhu, Hujun Bao, and Wewei Xu. 2022b. A Hybrid Mesh-neural Representation for 3D Transparent Object Reconstruction. *arXiv preprint arXiv:2203.12613* (2022).
- Qingshan Xu and Wenbing Tao. 2019. Multi-scale geometric consistency guided multi-view stereo. In *Proceedings of the IEEE/CVF Conference on Computer Vision and Pattern Recognition*. 5483–5492.
- Qingshan Xu and Wenbing Tao. 2020a. Planar prior assisted patchmatch multi-view stereo. In *Proceedings of the AAAI Conference on Artificial Intelligence*, Vol. 34. 12516–12523.
- Qingshan Xu and Wenbing Tao. 2020b. Planar Prior Assisted PatchMatch Multi-View Stereo. *AAAI Conference on Artificial Intelligence (AAAI)* (2020).
- Qiangeng Xu, Zexiang Xu, Julien Philip, Sai Bi, Zhixin Shu, Kalyan Sunkavalli, and Ulrich Neumann. 2022a. Point-NeRF: Point-based Neural Radiance Fields. *arXiv preprint arXiv:2201.08845* (2022).
- Jianfeng Yan, Zizhuang Wei, Hongwei Yi, Mingyu Ding, Runze Zhang, Yisong Chen, Guoping Wang, and Yu-Wing Tai. 2020. Dense hybrid recurrent multi-view stereo net with dynamic consistency checking. In *European Conference on Computer Vision*. Springer, 674–689.
- Jiayu Yang, Wei Mao, Jose M Alvarez, and Miaomiao Liu. 2020. Cost volume pyramid based depth inference for multi-view stereo. In *Proceedings of the IEEE/CVF Conference on Computer Vision and Pattern Recognition*. 4877–4886.
- Yao Yao, Zixin Luo, Shiwei Li, Tian Fang, and Long Quan. 2018. Mvsnet: Depth inference for unstructured multi-view stereo. In *Proceedings of the European Conference on Computer Vision (ECCV)*. 767–783.
- Yao Yao, Zixin Luo, Shiwei Li, Tianwei Shen, Tian Fang, and Long Quan. 2019. Recurrent mvsnet for high-resolution multi-view stereo depth inference. In *Proceedings of the IEEE/CVF Conference on Computer Vision and Pattern Recognition*. 5525–5534.
- Lior Yariv, Jiatao Gu, Yoni Kasten, and Yaron Lipman. 2021. Volume rendering of neural implicit surfaces. *Advances in Neural Information Processing Systems* 34 (2021), 4805–4815.
- Lior Yariv, Yoni Kasten, Dror Moran, Meirav Galun, Matan Atzmon, Basri Ronen, and Yaron Lipman. 2020. Multiview neural surface reconstruction by disentangling geometry and appearance. *Advances in Neural Information Processing Systems* 33 (2020), 2492–2502.
- Alex Yu, Sara Fridovich-Keil, Matthew Tancik, Qinhong Chen, Benjamin Recht, and Angjoo Kanazawa. 2021. Plenoxels: Radiance Fields without Neural Networks. *arXiv preprint arXiv:2112.05131* (2021).
- Zehao Yu, Songyou Peng, Michael Niemeyer, Torsten Sattler, and Andreas Geiger. 2022. MonoSDF: Exploring Monocular Geometric Cues for Neural Implicit Surface Reconstruction. *arXiv preprint arXiv:2206.00665* (2022).
- Jingyang Zhang, Yao Yao, Shiwei Li, Zixin Luo, and Tian Fang. 2020b. Visibility-aware multi-view stereo network. *arXiv preprint arXiv:2008.07928* (2020).
- Kai Zhang, Gernot Riegler, Noah Snavely, and Vladlen Koltun. 2020a. Nerf++: Analyzing and improving neural radiance fields. *arXiv preprint arXiv:2010.07492* (2020).
- Wenxiao Zhang, Zhen Dong, Jun Liu, Qingan Yan, Chunxia Xiao, et al. 2022. Point Cloud Completion Via Skeleton-Detail Transformer. *IEEE Transactions on Visualization and Computer Graphics* (2022).
- Qian-Yi Zhou, Jaesik Park, and Vladlen Koltun. 2018. Open3D: A Modern Library for 3D Data Processing. *arXiv:1801.09847* (2018).